Influence of Solidification Thermal Parameters on the Columnar-to-Equiaxed Transition of Aluminum-Zinc and Zinc-Aluminum Alloys

A.E. ARES and C.E. SCHVEZOV

Understanding the interaction between the parameters involved in the columnar-to-equiaxed transition (CET) has gained considerable attention over the last two decades in the study of the structure of ingot castings. The present investigation was undertaken to investigate experimentally the directional solidification of Al-Zn and Zn-Al (ZA) alloys under different conditions of superheat and heat-transfer efficiencies at the metal/mold interface. The CET is observed; grain sizes are measured and the observations are related to the solidification thermal parameters: cooling rates, growth rates, thermal gradients, and recalescence determined from the temperature *vs* time curves. The temperature gradient in the melt, measured during the transition, is between –0.338 °C/mm and 0.167 °C/mm. In addition, there is an increase in the velocity of the liquidus front faster than the solidus front, which increases the size of the mushy zone. The size of the equiaxed grains increases with distance from the transition, an observation that was independent of alloy composition. The observations indicate that the transition is the result of a competition between coarse columnar dendrites and finer equiaxed dendrites. The results are compared with those previously obtained in lead-tin alloys.

DOI: 10.1007/s11661-007-9111-z

I. INTRODUCTION

THE microstructure of Al-Zn and Zn-Al (ZA) ingot castings is of technological interest because the Al-Zn alloys combine the high wear resistance, heat resistance, and strength with the castability demanded for many aeronautic and automotive industrial applications.[1,2] Also, ZA alloys combine high strength and hardness, good machinability with good bearing properties, and wear resistance often superior to standard bronze alloys. The ZA castings compete with cast iron, bronze, and aluminum because of various property and processing advantages. All ZA alloys offer superior creep resistance and performance at elevated temperatures compared to standard zinc alloys and can be applied where bearing properties are important.[3–8]

In the present report, the focus is on the directional solidification of Al- and Zn-based alloys and, more particularly, on the columnar, equiaxed growth, and columnar-to-equiaxed transition (CET). Experimental evidence of the CET has been reported in previous articles,[9–25] and also a number of mechanisms for the phenomenon of the CET have been proposed.[26–47] It has been demonstrated that the CET is influenced by casting size, composition, and constitution of the alloy system, melt superheat, stirring, heat-transfer coefficient at the metal mold interface, inoculation, cooling rate of the mold, temperature gradient, *etc*.[11] Recently, Mangelinck-Noel *et al*.[25] obtained results on the CET by X-ray radiography.

In recent years, numerical modeling of the CET has been the subject of studies.[26–47] Essentially, it is possible to find two types of models: stochastic models[26,27,28] and deterministic models.[29–47] The combination of multiple factors and the complexity of phenomenon present difficulties for the total understanding and mathematical modeling of the CET.

In the present investigation, directional solidification experiments on aluminum-zinc and zinc-aluminum alloys are performed in order to measure the temperature fields during the transition, which are used to derive and analyze the most important parameters such as cooling rate, velocity of the liquidus and solidus fronts, local solidification time, temperature gradients, and recalescence. The evolution of these parameters is followed and contrasted with the grain structure obtained after solidification and with previous research in other alloy systems.[18,22,45]

II. EXPERIMENTAL

A. *Alloy Preparation*

Alloys of different compositions were prepared from aluminum (99.96 pct) and zinc (99.999 pct).

The directional solidification process was monitored by inserting six thermocouples in holes 3.0 mm in diameter

A.E. ARES, Research Assistant, and C.E. SCHVEZOV, Professor, are with the Consejo Nacional de Investigaciones Científicas y Técnicas, (CONICET)/Faculty of Sciences, Misiones State University, (3300) Posadas, Misiones, Argentina. Contact e-mail: schvezov@fceqyn.unam.edu.ar

This article is based on a presentation made in the symposium entitled "Solidification Modeling and Microstructure Formation: in Honor of Prof. John Hunt," which occurred March 13–15, 2006 during the TMS Spring Meeting in San Antonio, Texas, under the auspices of the TMS Materials Processing and Manufacturing Division, Solidification Committee.

Article published online May 25, 2007.

and 7.0 mm in depth drilled in the alloy sample. The separation distance between thermocouples was 20.00 mm, and the first was located at 45 mm from the base of the sample. Previous to inserting the thermocouples, the alloy was deoxidized with a solution containing $8.5H_2O$: $1.0HCl$:$0.5HNO_3$.[48] The thermocouples were protected with a refractory paste. The samples were solidified in alumina tubes 16.00 mm in diameter and 200 mm in length. The thermocouples were inserted in the sample through respective holes drilled in the alumina tube.

B. *Directional Solidification*

The alloys were solidified directionally upward in an experimental setup consisting of a heating unit, a temperature control system, a temperature data acquisition system, a sample moving system, and a heat extraction system. Initially, the melt was allowed to reach the selected temperature, and then, the furnace power was turned off and the melt was allowed to solidify from the bottom. Heat was extracted through a cooling system, which consisted of a copper cylinder cooled by running water, as you can see in a schematic representation of the experimental setup (Figure 1).

The solidification velocity was adjusted by changing the flow of water and also changing the material of cylinder, using a 316 L stainless steel cylinder, which changed the effective value of the thermal conductivity. The data were acquired automatically using K type thermocouples (external diameter (e.d.) 2 mm) connected to a data logger.

C. *Temperature Measurements*

During the solidification process, temperatures at different positions in the alloy sample were measured. For the measurements, a set of six arranged thermocouples was used. After many experiments, under very dissimilar conditions, we consider that the thermocouple set under the experimental conditions does not considerably affect the local process and also that the temperature readings are good enough to capture the main characteristics of the phenomena occurring during the transition, particularly because the gradients are very shallow, which results in small local heat flows that mostly occur in the axial direction. Moreover, during the transition, the phenomenon is controlled locally and not by external factors such as the heat input or output.

During a solidification experiment, the temperature measured by each thermocouple was recorded at regular intervals of time. Different intervals were previously tested, and as a result of this exercise, an interval of 1 second was selected. For the data processing, the readings made every 0.10 seconds during 1 second were averaged, and this value was associated to the middle of the averaged interval. This procedure was chosen as a result of a compromise between memory available in the data logger, the time taken for an entire solidification experiment, and the degree of precision to capture the main phenomena occurring during the transition.

D. *Metallography*

The solidified alloys were cut in the longitudinal direction, which is parallel to both the sample axis and the direction of solidification. After this, the samples were polished with emery paper up to 1200 grit and with 6-μm and 1-μm diamond paste. Etching was performed for aluminum-zinc alloys using a solution

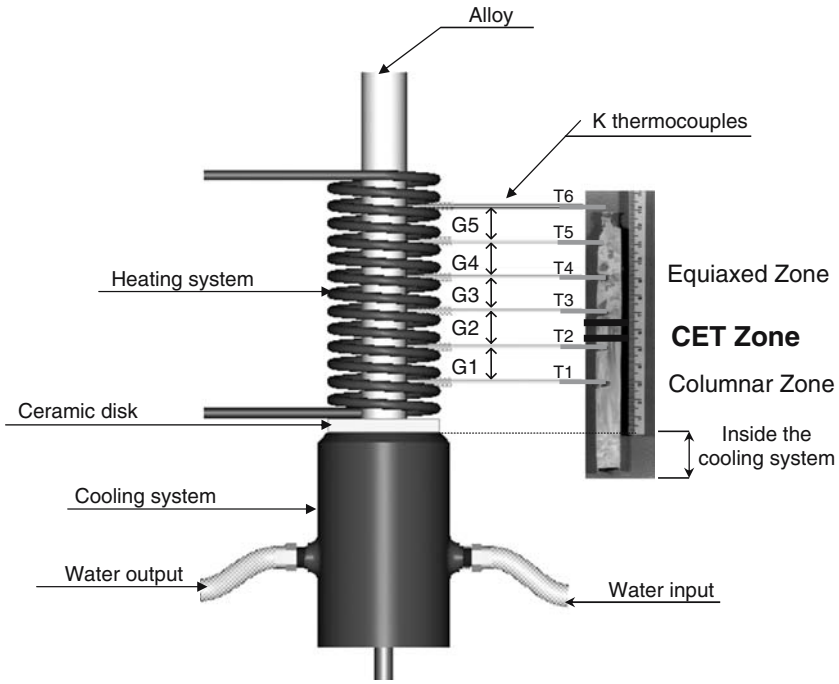

Fig. 1—Schematic of experimental setup.

consisting of 320 mL HCl, 160 mL HNO_3 during approximately 10 seconds at room temperature (25 °C); for zinc-aluminum alloys using concentrated hydrochloric acid during 3 seconds at room temperature, followed by rinsing and wiping off the resulting black deposit; and for microstructures with a mix containing chromic acid (50 g Cr_2O_3 and 4 g Na_2SO_4 in 100 mL of water) during 10 seconds at room temperature.[48] The position of the transition was located by visual observation and optical microscopy, and the distance from the bottom of the sample was measured with a ruler. The grain size in the equiaxed and columnar zone was determined from micrography using a standard technique.[49]

III. RESULTS

A. *CET Observations*

Thirty experiments in a range of alloy composition and cooling rates were performed; the list of compositions is shown in Table I. The compositions cover a wide range from Al-2 wt pct Zn to Al-50 wt pct Zn and from Zn-2 wt pct Al to Zn-27 wt pct Al. Table I also shows the position of the transition from the bottom of the sample. Typical results of the transition are shown in Figure 2(a) for Al-2 wt pct Zn alloy and in Figure 2(b) for Zn-2 wt pct Al alloy. It is noted that the melted zone in the experiment starts at the region marked as the chill zone. In the samples, which correspond to Al-Zn alloys, it was observed that the equiaxed grains are larger than in the ZA alloys samples, where the number of columnar as well as equiaxed grains is small.

The CET is not sharp, showing a zone where some equiaxed grains coexist with columnar grains. The size of the transition zone is on the order of up to ten millimeters. It is important to note at this point that no effect of the set of the thermocouples in the transition is observed, either acting as nucleating sites or changing the solidification structure. Similar results were found for Pb-Sn alloys using another experimental setup.[18,22]

Table I. Alloy System, Average Cooling Rate in the Melt (Calculated as the Slope of the Temperature Curve in the Cooling of the Melt and Averaging These Values), Corresponding Length of Columnar Zone (Minimum and Maximum), and Observations: Temperature Gradients in the Liquid Phase, $G_{L\ (\mathrm{CRITICAL})}$, and Liquidus Interface Velocity, $V_{L\ (\mathrm{CRITICAL})}$, Both Calculated at the Moment of the CET

No.	Alloy	Average Cooling Rate (°C/S)	Minimum Columnar Length (mm)	Maximum Columnar Length (mm)	$G_{L\ (\mathrm{CRITICAL})}$ (°C/mm)	$V_{L\ (\mathrm{CRITICAL})}$ (mm/S)
Al-Zn Alloys						
1	Al-2 wt pct Zn	3.14	32	46	−0.009	1.4
2		1.93	22	36	−0.052	1.2
3		1.87	24	32	−0.063	1.0
4		1.55	19	35	−0.154	1.0
5		2.46	27	55	0.091	1.1
6	Al-4 wt pct Zn	2.64	24	106	−0.123	1.8
7		2.80	25	37	−0.152	1.2
8		2.25	23	33	−0.022	1.2
9		1.96	20	30	−0.167	1.6
10		1.78	8	24	0.139	1.6
11	Al-16 wt pct Zn	2.95	35	45	0.036	1.6
12		3.26	52	61	−0.033	1.7
13		3.18	39	51	−0.075	1.8
14		3.06	35	47	0.041	2.1
15		2.72	31	38	0.102	2.4
16	Al-50 wt pct Zn	3.62	76	100	−0.186	1.6
17		2.90	42	66	−0.036	1.7
18		2.81	38	44	0.009	1.8
Zn - Al Alloys						
1	Zn-2 wt pct Al	1.72	69	91	0.091	2.8
2		2.46	60	75	−0.107	1.4
3		2.80	32	44	−0.338	1.3
4	Zn-4 wt pct Al	1.77	18	26	−0.049	1.6
5		2.21	40	60	−0.031	2.8
6		2.63	68	79	−0.009	1.0
7	Zn-16 wt pct Al	2.18	11	22	0.167	1.6
8		3.78	26	39	−0.046	1.7
9		2.84	19	30	−0.21	1.8
10	Zn-27 wt pct Al	2.43	23	43	−0.125	1.5
11		2.15	18	28	0.055	2.1
12		3.5	39	65	−0.068	1.9

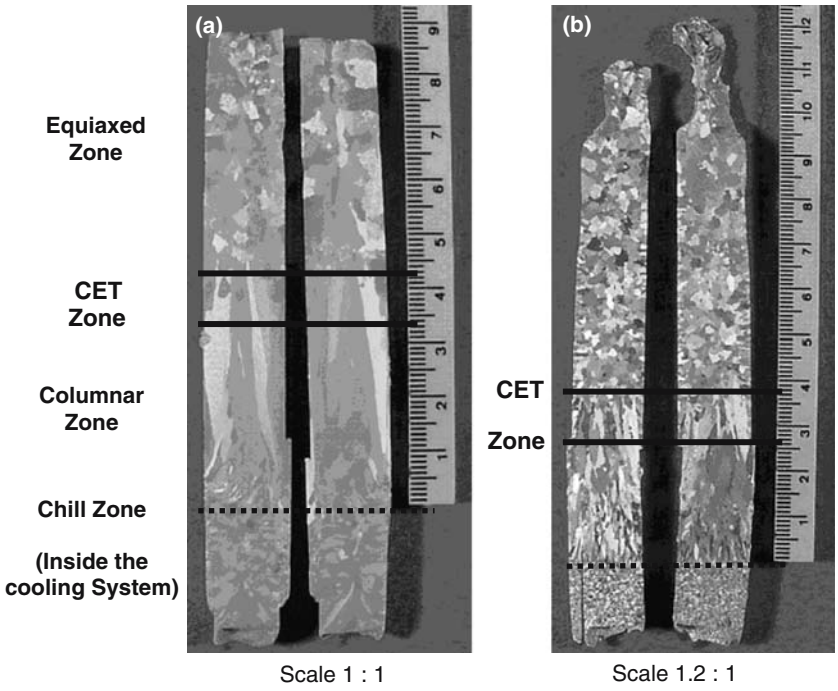

Fig. 2—Macrographs of (*a*) Al-2 wt pct Zn (scale 1:1) and (*b*) Zn-2 wt pct Al (scale 1.2:1) alloys.

B. *Temperature Measurements*

The temperatures measured by the six thermocouples inserted in the sample during the entire process were stored and analyzed for all the experiments. A typical time-dependent temperature plot for the six thermocouples in a sample with a CET is shown in Figures 3(a) through (d) for four different alloy concentrations. The thermocouple T_1 is at the lowest position and the first to reach the solidification front, and T_4, T_5, or T_6 is at the highest position. In Figure 3(a), only the recordings of four thermocouples are shown because the other two did not record the temperatures properly (T_5 and T_6). The same happened with thermocouple T_6 in Figures 3(b) and (d).

In all the curves, it is possible to identify a period corresponding to the cooling of the melt, a second period of solidification, and the final period of cooling of the solid to ambient temperature. Also, it is possible to identify a short period of recalescence when the CET occurs at a thermocouple position.

The temperature *vs* time curves also show that the temperature evolution depends on the structure being formed. During columnar solidification, the temperature decreases steadily and monotonically (generally, T_1 and T_2 in the temperature *vs* time curves); on the contrary, in the CET and equiaxed regions, the behavior of each curve shows that the temperature readings from the curves are very close to each other, resulting in low-temperature gradients.

In addition, as was commonly observed in some of the samples, there is some cooling from the top, which results in temperatures at the top that may be lower than the temperatures below (this is the case of T_6 in Figure 3(c)).

Moreover, increasing the alloy content, the temperature for the beginning of solidification decreases and changes the difference between the liquidus line temperature, T_L, and the solidus line temperature, T_S, that is, $\Delta T = T_L - T_S$; it is possible to observe the comparison of Figures 3(a) and (b) for Al-Zn alloys and Figures 3(c) and (d) for ZA alloys.

The results, which are shown in Figure 3, are within the predicted values given by the phase diagram for the alloys studied[50] (Figure 4).

C. *Solidification parameters*

From the data shown in Figure 3, the following information can be extracted: melt superheat, cooling rate of the melt, position of the solidification fronts for the solidus and the liquidus temperature, local solidification time, velocity of both solidification fronts, length of the mushy zone, and cooling rate of the solid and temperature gradients. In some cases, the quantification of this information is straightforward, like the case of melt superheat, which is the highest temperature above the liquidus reached by the melt before the furnace is turned off. It is also the case of the cooling rate, which is calculated as the slope of the temperature curve in both periods refer to (a) the cooling of the melt and (b) the cooling of the solid. The positions of the solidification fronts *vs* time are determined by the start and the end of solidification at each thermocouple, which correspond to the liquidus and the solidus temperatures, respectively. Both points are detected by the changes in the slopes of the cooling curve at the start and end of solidification. This criterion was chosen in order to allow undercooling to occur before solidification and

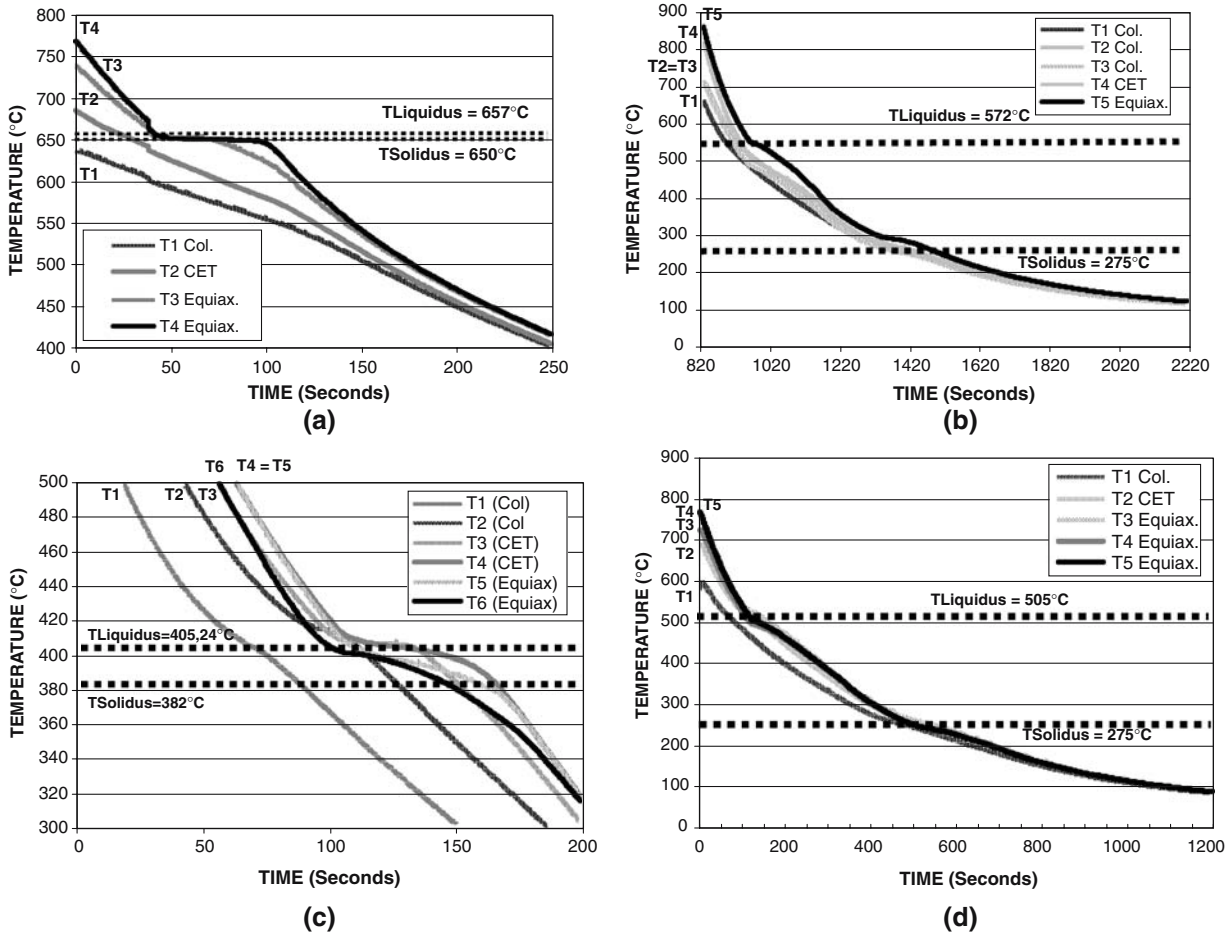

Fig. 3—Temperature *vs* time curves: (*a*) Al-2 wt pct Zn, (*b*) Al-50 wt pct Zn, (*c*) Zn-2 wt pct Al, and (*d*) Zn-27 wt pct Al.

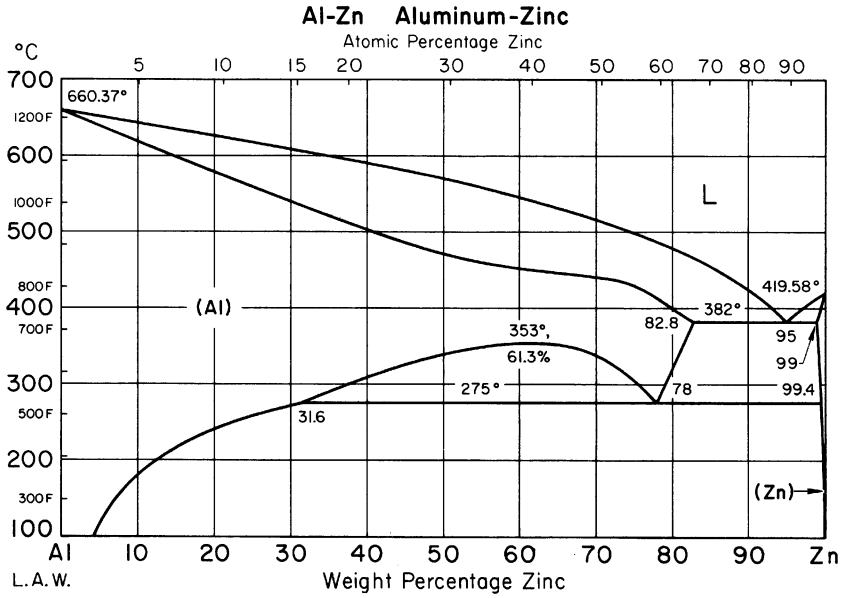

Fig. 4—Zinc-aluminum phase diagram[50].

possible recalescence during solidification of equiaxed grains, because this process is characterized by nucleation and solidification of grains in the melt rather than for what is observed in a normal solidification process where there is a dendrite tip front advancing in the melt. The local solidification time at each thermocouple location is determined by the period of time taken for the temperature to go from the liquidus to the solidus temperature.

The velocity of the solidification fronts is calculated as the distance between the thermocouples divided by the time taken by either the liquidus or solidus temperature to go from the lower to the upper thermocouple. These velocities are named as v_L and v_S for the liquidus and solidus velocity, respectively.

The temperature gradients at all times are calculated in a straightforward fashion, dividing the temperature difference between two thermocouples by the separation distance between them.

The error in the temperature readings, considering the average procedure and the sensitivity of the data logger in the digital process, is $\Delta T = 0.5$ °C. In the case of the distance between thermocouples, the error of appreciation is $\Delta x = 1$ mm from which the relative error in the measurement of the gradients results to be $\frac{\Delta G}{G} = \frac{1}{(T_{i-1} - T_i)} + 0.04$, where the fact that the separation between thermocouples is 20 mm is used. For instance for a gradient of 0.2 °C/mm, the uncertainly of this value is of the order of 0.06 °C/mm. However, the calculated gradients are listed with four decimal digits for reference purposes only.

1. *Effect of cooling rate on the length of the columnar zone*

In order to correlate the length of the columnar zone with practical parameters, we determined regressions equations; these equations are useful in modeling the length of the columnar zone. Using the temperature data obtained in the experiments with Al-Zn alloys in which different columnar lengths were obtained, the average cooling rate in the melt is calculated. The cooling rate is $\dot{T}$, calculated employing the data from the upper thermocouples and averaging these values. The results are shown in Figure 5, where for each cooling rate the maximum columnar lengths, $L_{\text{col.}}$, are presented.

This result shows the strong effect of cooling rate in the melt on columnar length. In addition, by extrapolating the lines to the abscise in Figure 5, it is possible to predict the minimum cooling rate for which columnar growth is no longer possible and the resultant structure is fully equiaxed; this value is shown in Figure 5 by the vertical line.

With respect to melt superheat, the results show no correlation with columnar length, which are in agreement with the results reported by Mahapatra and Weinberg[11] and Ares and Schvezov[18] previously.

2. *Effect of solute concentration on the length of the columnar zone*

In order to determine the effect of alloy composition on the length of the columnar zone, it is necessary to consider the results obtained under similar cooling rates.

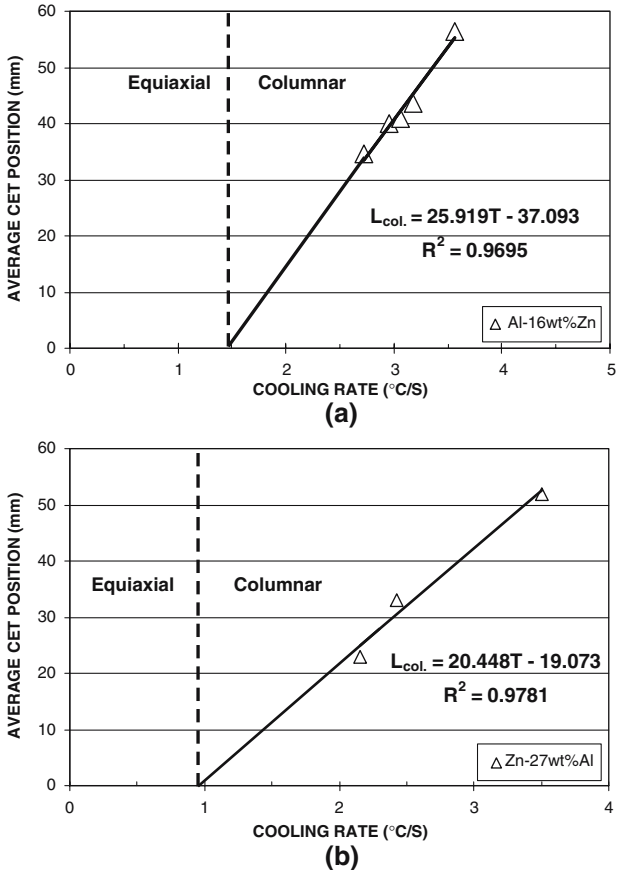

Fig. 5—Length of the columnar zone *vs* cooling rate for (*a*) Al-16 wt pct Zn and (*b*) Zn-27 wt pct Al.

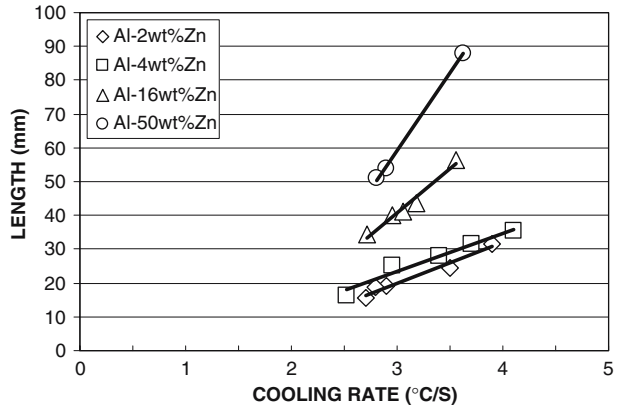

Fig. 6—Effect of the concentration on the length of the columnar zone. Al-Zn alloys.

This is possible to do comparing the results for Al-2 wt pct Zn and for Al-16 wt pct Zn with similar cooling rates (3.5 °C/s), which result in columnar zones of 25 and 55 mm, respectively; that is, in this case, increasing the concentration, the length of the columnar zone increases (Figure 6). Similar results were obtained for ZA alloys (Figure 7).

Alternatively, to produce a given columnar length, increasing the zinc content in the alloy (Figure 6) and the aluminum content in the alloy (Figure 7) requires a

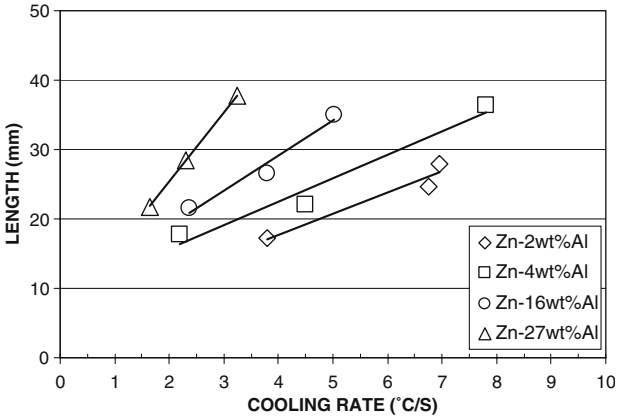

Fig. 7—Effect of the concentration on the length of the columnar zone. ZA alloys.

reduction in cooling rate. It must be noted here that this effect occurs under vertical solidification and for these alloys.

3. *Temperature gradients*

The temperature gradients calculated from the readings from the five thermocouples for Al-50 wt pct Zn are shown in Figure 8. They are referred to as G_1, G_2, G_3, and G_4. The period of time is 300 seconds (5 minutes), which comprises the entire solidification process including the transition.

The vertical lines in Figure 8 show the time at which the liquidus front reaches each thermocouple position; the line T_1 coincides with the vertical axis and corresponds to the origin of the time axis. In 108.90 seconds, the liquidus front reaches the T_2 thermocouple position.

In 124.96 seconds, the liquidus front reaches the T_3 thermocouple position, which is the time when the transition at T_3 occurs. At the beginning, the gradients are larger with values between 3 °C/mm and 3.5 °C/mm at the bottom of the sample, G_1 and G_2, respectively, and around 0.6 °C/mm at the top (G_4). These values gradually decrease; when the transition occurs, the gradient in the liquid becomes small and slightly negative (−0.1865 °C/mm). After this, the gradients increase during the final cooldown of the solid. Similar behavior can be observed in all the samples. The values for all the experiments are listed in Table I. The scatter in the values of the gradient is associated with the fact that the transition usually occurs between two thermocouples, and therefore, the calculated value is an average value over a region that includes the mushy zone and the melt. In addition, according to the relative error presented previously, at these low values of temperature, differences of error in the calculated gradients could be as large as 45 pct. Thereby, taking into account these considerations, it can be concluded that, within the error, the alloy composition does not have an effect on the temperature gradient during the transition.

Comparing in Figure 8 the separation in time (x-axis) between the vertical lines, which determines the time when the liquidus point reaches the position of the corresponding thermocouple, it is observed that between T_1 and T_2, there are 108.90 seconds; between T_2 and T_3, 16.06 seconds; and between T_3 and T_4, only 4.40 seconds. This shows, first, that there is an acceleration of the liquidus interface and, second, that the transition occurs not only at low gradient but also with large velocities.

According to these, both the temperature gradients and liquidus interface velocity are calculated for all the experiments performed and correlated with the type of structure, columnar or equiaxed, present for each pair of values, and they are represented in a G_L *vs* $v_L$graph. The result is shown in Figure 9, where three regions can be defined: a fully equiaxed region for high velocities and low gradients, a fully columnar region for large gradients and small velocities, and a mixed equiaxed and columnar region separating the other two regions. These results indicate that both velocity and gradient are critical parameters determining the CET. In the same figure, it is possible to observed the prediction of the Hunt model[34] with the undercooling at the heterogeneous nucleation temperature, $\Delta T_N = 0.75$ K, and the number of particles that have already nucleated, $N = 100\ \text{cm}^{-3}$.

Moreover, in the case of the liquidus interface velocity at the moment of the CET, it is found that it is possible

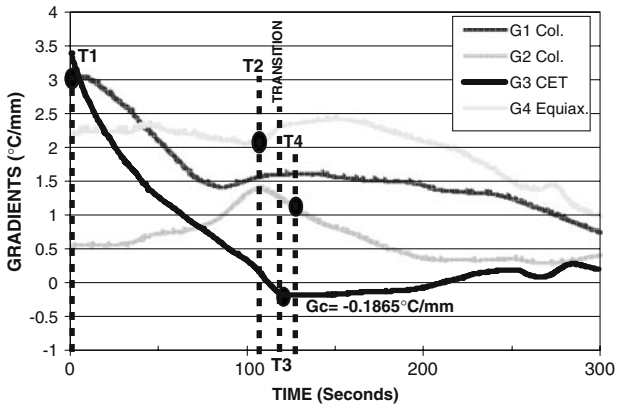

Fig. 8—Temperature gradients ahead of the liquidus interface. 50 wt pct Zn alloy.

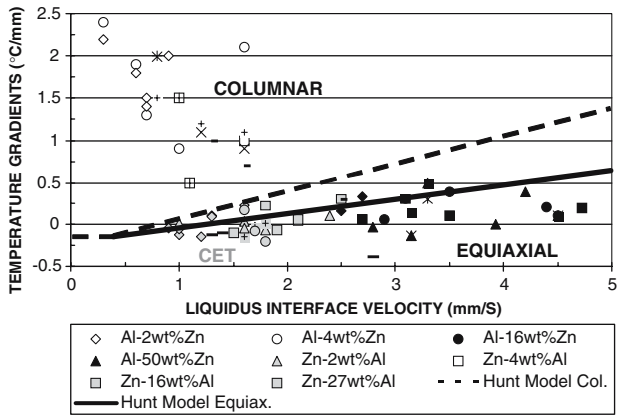

Fig. 9—Temperature gradients in the liquid *vs* velocity of liquidus interface.

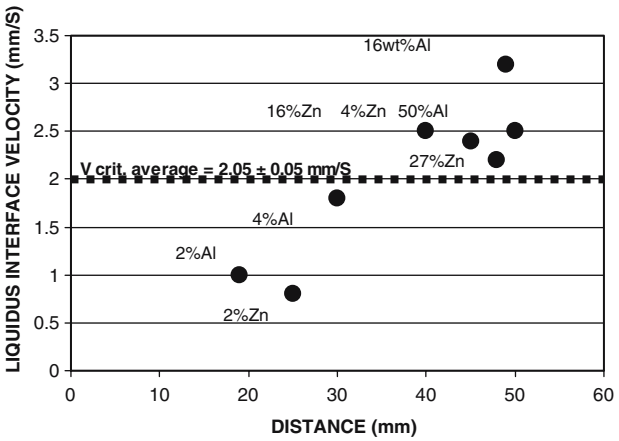

Fig. 10—Critical velocity *vs* distance from the chill.

to establish a critical average value for the Al-Zn and ZA alloys, which is about 2.05 ± 0.05 mm/s. This value is independent of the position of the transition, *i.e.*, distance from the chill, and alloy composition. This is shown in Figure 10 for eight experiments. It is noted that the lower concentration alloys Zn-2 wt pct Al, Al-2 wt pct Zn, and Zn-4 wt pct Al have velocities below the average, and the remaining higher concentration alloys have velocities higher than the average, indicating that, for a given gradient, larger or thicker (blunter) dendrites can normally grow at lower velocities than thinner dendrites, which, on the other hand, and under a pronounced reduction of the growth velocity should switch to a thicker (blunt) morphology, which could result more difficult to occur.

4. *Recalescence*

In the experiments where the transition occurs, an effect of recalescence is normally observed. The characteristics of this observation can be described using the inset of Figure 11. This figure represents an enlargement of a short period of time of a region of Figure 11 for the thermocouple T_2 measured during one experiment with Zn-4 wt pct Al alloy. The thermocouple encloses a region in the sample, which corresponds to the transition to equiaxed structure. The separation between thermocouples is 20 mm. In Figure 11, the temperature readings show that, after the start of the transition that occurs after 536 seconds in the plot, there is a slight increase in temperature above the plateau, after reaching a minimum value. This increase is of approximately 0.625 °C. The duration of this recalescence is short, lasting a few seconds (20 seconds approximately); however, the region affected could be larger than the separation between thermocouples. Similar effects are observed in other thermocouples in which the transition occurs close to a thermocouple.

The average recalescence ranges for different alloys are presented in Table II. It is noted that the Al-Zn alloys have higher recalescence than the ZA alloys; however, due to the large scatter, this cannot be firmly stated.

D. *Dynamics of Solidification*

It has been shown in previous research[18,22,45] that, during the solidification of an alloy, including the CET, the more important parameters are the velocities of the liquid and solid fronts, local solidification time, and temperature gradients ahead of the interface. In this section, these parameters are calculated and analyzed for Al-Zn and ZA alloys from the temperature measurements from fixed observation points. Also, another complementary way of showing the dynamic of the transition is done through a time-dependent sequence of temperature profiles.

The solidification velocity is not constant. By carefully following both fronts as they pass the thermocouples, it is possible to determine the position of both fronts as a function of time and their velocities, which can be determined as a function of time and position. A typical result of the position of the liquid front as a function of time is represented in Figure 12. It can be noted that

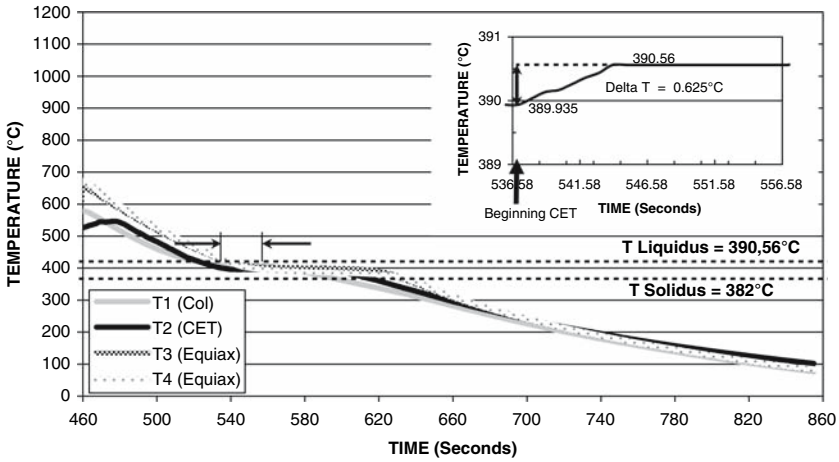

Fig. 11—Temperature *vs* time dependence. Zn-4 wt pct Al alloy.

Table II. Alloy, Average Recalescence, and Diameter of the Equiaxed Grains Which Solidify During the Massive Nucleation

Alloy	Average ΔT (°C) (Recalescence)	$d = \sqrt[3]{\frac{6C_p\Delta T}{\lambda N\pi}}$ (μm) (with $N = 10{,}000$ cm^{-3})	$d = \sqrt[3]{\frac{6C_p\Delta T}{\lambda N\pi}}$ (μm) (with $N = 1000$ cm^{-3})	$d = \sqrt[3]{\frac{6C_p\Delta T}{\lambda N\pi}}$ (μm) (with $N = 100$ cm^{-3})	$d = \sqrt[3]{\frac{6C_p\Delta T}{\lambda N\pi}}$ (μm) (with $N = 50$ cm^{-3})	Average Actual Grain size, d (μm)
Al-2 wt pct Zn	0.625	69.63	1472	5873	4072	5933
Al-4 wt pct Zn	1.375	90.66	1953	4208	5302	4475
Al-16 wt pct Zn	1.035	83.03	1789	3854	4856	3950
Al-50 wt pct Zn	1.01	84.65	1824	3929	4950	3105
Zn-2 wt pct Al	0.595	77.87	1678	3615	4554	1612
Zn-4 wt pct Al	0.535	74.64	1608	3465	4365	1754
Zn-16 wt pct Al	0.74	80.46	1733	3735	4706	1813
Zn-27 wt pct Al	0.76	79.43	1711	3687	4645	1324

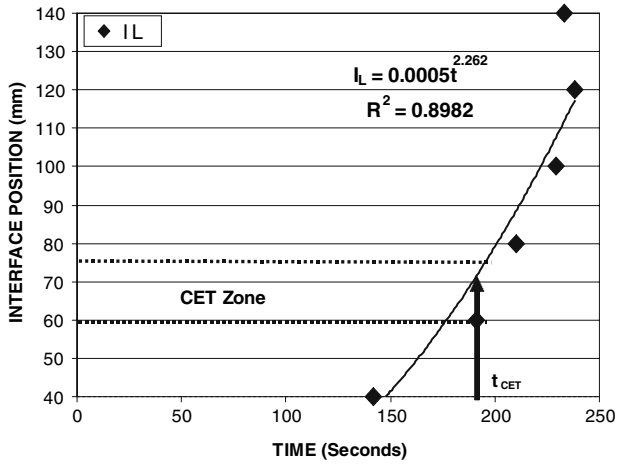

Fig. 12—Position of the liquid front *vs* time. Zn-2 wt pct Al alloy.

after 200 seconds, the position of the liquid interface advances very fast. The solid front moves well behind the liquid front at a speed, which up to the transition, is similar to the velocity of the liquid front and accelerates much less than the liquid after the transition. The position of the liquid interface can be fitted by a potential function as $I_L = 5{*}10^{-4}t^{2.262}$, where I_L = mm and t = s. The velocity can be derived from this potential function as $v_L = 1{\cdot}10^{-5}I_L^{2.9752}$ mm/S, valid for 4 cm $\leq I_L \leq$ 10 cm.

The velocity of the solid front, on the other hand, remains low. Both velocities are represented in Figure 13. It is observed that, as a result of this, the size of the mushy zone increases very fast. Moreover, there is a specific direction of motion of the interface, which is the upward direction indicating that heat extraction is from the bottom and that nucleation of new grains after the transition is in a cascade mode rather than as a fully homogeneous nucleation mode. This pattern is observed in all experiments in which the transition leaves enough equiaxed regions to acquire data for this kind of analysis.

The local solidification time, as defined previously, is represented in Figure 14 for a number of experiments

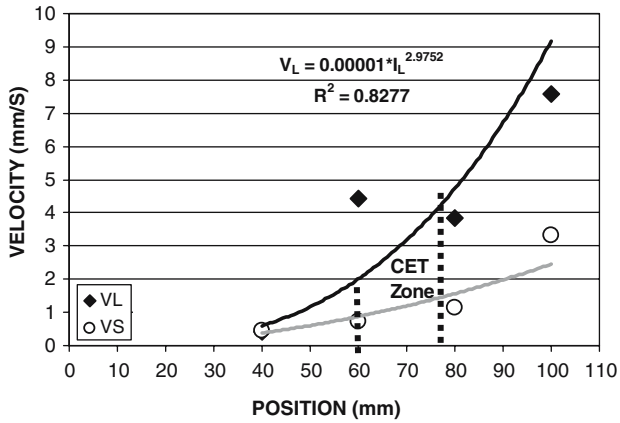

Fig. 13—Velocities of the liquid and solid fronts. Zn-2 wt pct Al alloy.

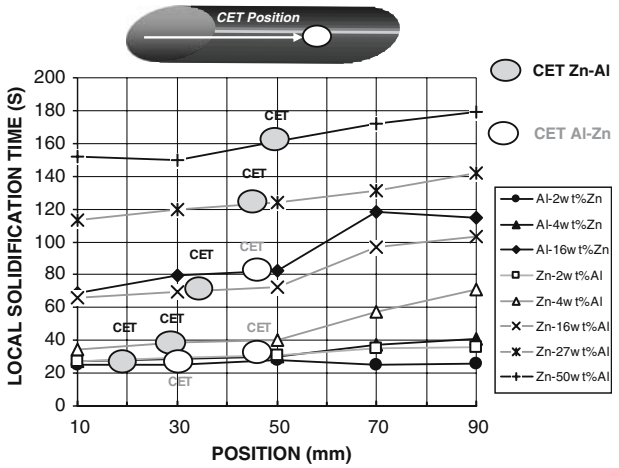

Fig. 14—Local solidification time *vs* position.

covering the entire range of compositions employed. The behavior of this parameter may be described from two points of view. On one hand, at a given composition, it normally increases after the transition, as can be observed in most experiments.

On the other hand, the solidification time notably increases with the content of the alloy. This may be explained taking into account the phase diagram (Figure 4), which shows larger differences between the liquidus and the solidus temperatures for the Al-Zn alloys, taking a longer time to reach the solid temperature and considering that the heat flux does not substantially differ among the experimental results in a longer time for solidification. On the other hand, and for the opposite side of the diagram, the longer local solidification time could be attributed to the presence of a eutectic with more complex solidification morphology,[8] thermal properties of the constituents, and also the latent heat of solidification of the alloy and the eutectic.

The temperature profiles that result from the temperature *vs* time graphs show a regular large positive gradient at the start of solidification, then the profiles begin to flatten, and finally the positive slopes are again restored to the end of solidification. It is during the transition that the temperature fields present particular features, such as the effect of recalescence discussed in Section B. It is of particular relevance to analyze the profiles during the transition.

The temperature profiles in all the sample lengths and at several times are shown in Figures 15(a) through (c). In this sample, the CET occurs at 50 mm from the base of the sample at about 258.62 seconds. The interval of time represented in the figures corresponds to the start of solidification at thermocouple 1 at 88.32 seconds (Figure 15(a)) up to the time 334.01 seconds (Figure 15(c)); the temperature gradient after this begins to be positive again all along the sample. This interval also includes the time it takes the CET to occur (Figure 15(b)).

The profile in Figure 15(a) shows in all cases a nearly constant gradient in the melt ahead of the interface when the spatial dimension is considered. With time, the

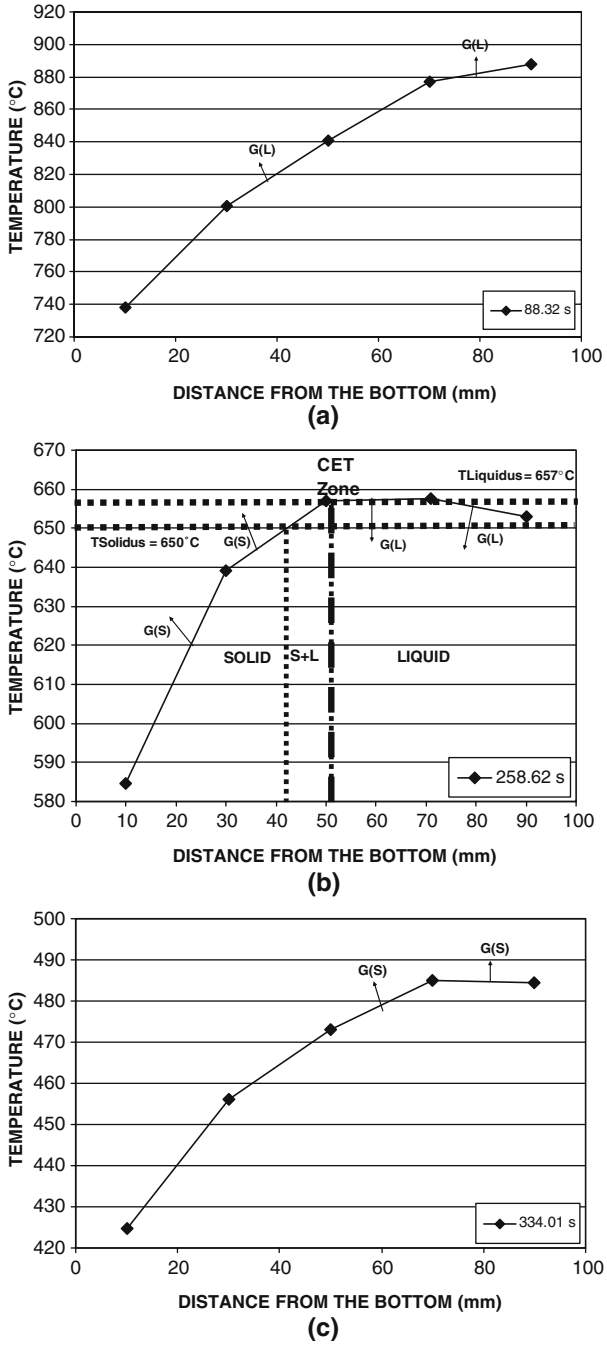

Fig. 15—Temperature profile *vs* time. Al-2 wt pct Zn: (*a*) 88.32 s, (*b*) 258.62 s, and (*c*) 334.01 s.

gradient decreases smoothly between 84.92 and 88.32 seconds. In Figure 15(b), when the CET structure is already progressing at 50 mm from the base, the temperature profiles have completely changed in shape, showing a positive gradient in the solid and a negative gradient across the position of the start of the transition where the interface is located. In addition, superimposed to the profiles, there are two sets of arrows: a thin set indicating the position of the liquid front, and a thick set showing the temperature gradient in the liquid ahead of the front in that region. The profiles until the beginning

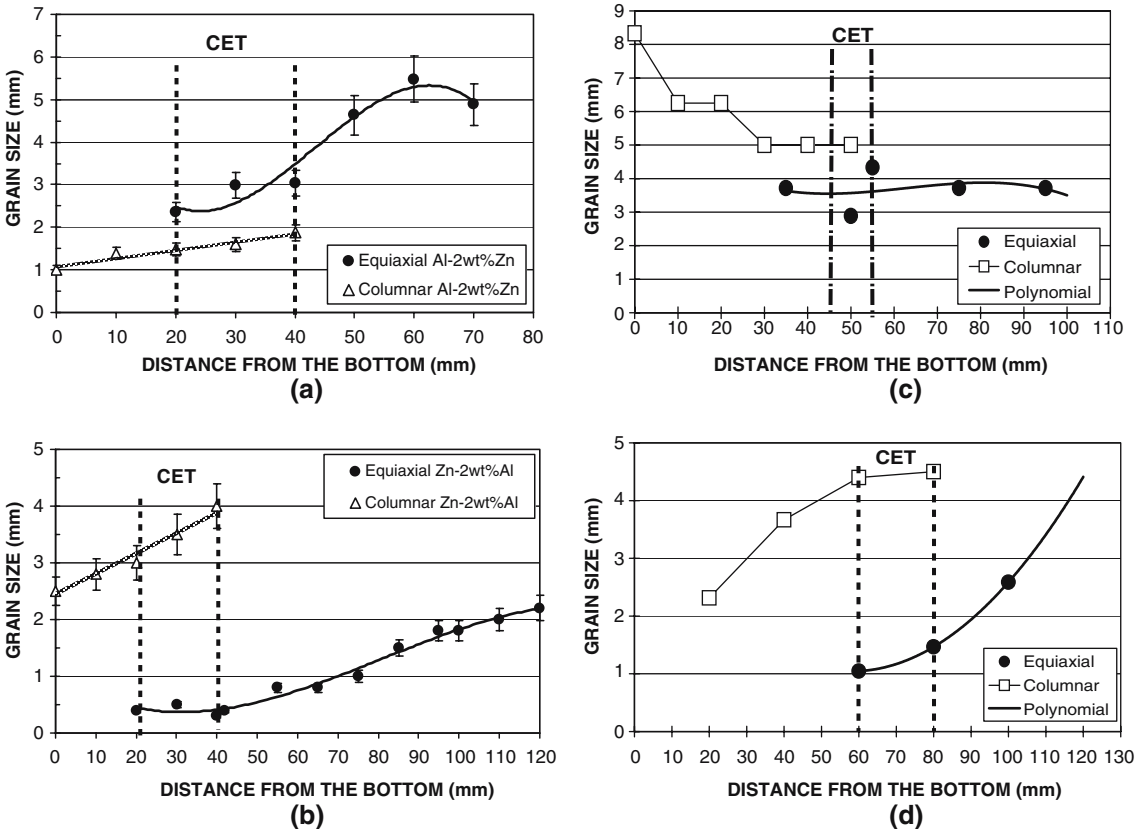

Fig. 16—Grain size measured *vs* distance: (*a*) Al-2 wt pct Zn, (*b*) Zn-2 wt pct Al, (*c*) Pb-4 wt pct Sn,[18] and (*d*) Al-7 wt pct Si.[51]

of the transition present positive gradients, and at 258.62 seconds, when the transition occurs, there is a negative gradient ahead of the liquidus interface of –0.009 °C/mm. Because the transition occurs right at this thermocouple position, the measured gradient is closer to the real gradient ahead of the interface. It could locally be larger because of the averaging in space and time. Negative gradients are normally measured when the thermocouple position is closer to the transition.

The profiles after the transition has occurred progressively restore the initial profile of positive gradient along the length of the region being considered (Figure 15(c)).

E. *Grain Size Measurements*

The equiaxed grain size was measured using the ASTM E112 standard norm,[49] at equally spaced intervals. The columnar region was divided in similar ways, and the width and length of the grains were measured directly.

The results, which also include the width of the columnar grain, are plotted as a function of position in the solidified sample for four samples in Figure 16. In Figure 16(a), the size of the equiaxed grains is 3 mm in the transition region and then starts to monotonically increase to a value of 5.5 mm at the end of the sample. In the case of the width of the columnar grains, it is observed that they increase in size from 1 to 2 mm at the transition region. A similar analysis was performed for a total of 30 solidification experiments. In Figure 16, only two of them are presented, corresponding to Figures 16(a) and (b). In addition, two more results are presented as Figures 16(c) and (d), which were produced with data obtained from published micrographs from Ares and Schvezov in Pb-4 wt pct Sn[18] and Gandin and Rappaz[51] in Al 7 wt pct Si. The points in the figures were fitted to polynomial functions of third degree.

The grain size was measured for both the equiaxed and columnar zones; in the latter, rather than the size, the width of the grain was measured, which for the purpose of this work could be better correlated with the nucleation phenomenon.

In Figure 16, it is observed that, in the transition, the size of the equiaxed grains is smaller than the width of the columnar grains except in the case of Figure 16(a) for Al-2 wt pct Zn. In the case of Al-Zn alloys, there are no substantial differences between the size of the columnar and the equiaxed grains at the moment of the CET, as is possible to observe in Figure 16(a). In this case, it is possible to appreciate the highest differences between sizes of different types of grains in Al-Zn alloys. The addition of Zn makes the nucleation of new aluminum grain difficult, indicating that the addition of Zn does not promote the nucleation of equiaxed grains.

However, in all cases, the size increases after the transition. At the end of solidification, the size may also decrease after reaching a maximum value. This behavior was previously reported in experiments with lead-tin alloys[18,22,45] and from micrographs published by Lowe,[52] Mahapatra,[11] and Biloni[53] for different alloy systems.

Another observation that is common to all the cases presented here is that the equiaxed grain size evolution is independent of the position of the transition, *i.e.*, length of the columnar region, type of alloy, alloy composition, or relative size of the equiaxed grains. It is observed that in the Al-Zn alloys the grain size is 1.5 to 2.5 mm, while for the ZA alloys, the size is smaller, less than 1 mm. This indicates a higher density of nuclei in the ZA alloys.

IV. DISCUSSION

In Sections III-D and III-E, the CET structure has been characterized focusing on two relevant aspects: the thermal and the structural. The thermal aspect has been studied using the temperature measured during solidification and cooling, while studies on the structural aspect consisted of the grain size distribution, which results after the solidification process. The main challenge so far is to correlate both aspects.

Some of the thermal parameters such as the cooling rate considered are of practical application. In practice, the correlation between the cooling rate with columnar length results is easier to realize. The correlation shows that the columnar length also depends on alloy composition; increasing composition results in a longer columnar length for a given cooling rate. On the other hand, there is no indication that this effect is the result of different critical gradients or heat flux for the transition, because these two parameters are essentially the same for all alloy compositions.

This effect may not be attributed to a nucleation phenomenon, because the equiaxed grain structure, as shown in Figure 16, does not appreciably change with alloy composition.

The scatter in the values of critical temperature gradient is attributed to the position of the thermocouples with respect to the position of the transition that changes from experiment to experiment. When both positions are close, there is an observation of recalescence, which is sensed in a region of about 20 mm at the solidification front; in some cases, there is also a negative gradient. Both phenomena start simultaneously; for instance, in Figure 15(b), the negative gradient is observed at 258.62 seconds, coinciding with the beginning of both the transition and the recalescence. Recalescence is the effect of release of heat, whose origin can be latent heat from nucleation and solidification of new grains and from coarsening of the dendrites.[54]

The amount of recalescence is an indication of the massive character of the nucleation and growth of equiaxed grains during the transition in a zone ahead of the liquid front. If it is assumed that all the heat comes from nucleation and solidification of new grains and that the densities of the solid and melt are the same, the diameter of the grains that solidify during this massive nucleation and growth of equiaxed crystals is $d = \sqrt[3]{\frac{6C_p\Delta T}{\lambda N\pi}}$. Using the average recalescence and the thermophysical properties of each alloy listed in Table - III, it is possible to observe for different alloy concentrations the respective size of the equiaxed grains for $N = 10{,}000\ \text{cm}^{-3}$, $N = 1000\ \text{cm}^{-3}$, $N = 100\ \text{cm}^{-3}$, and $N = 50\ \text{cm}^{-3}$ in Table II. Also, we compared these values with actual grain size. It is noted from the table that the best fit for Al-Zn alloys is with $N = 100\ \text{cm}^{-3}$ and for ZA alloys is with $N = 1000\ \text{cm}^{-3}$.

This growth is undoubtedly the result of a slowdown in the growth velocity of the columnar dendrites and the presence of an undercooled melt. What remains to be answered is if this growth of grains is in competition with the growth of the columnar dendrites or is the result of a stop in the growth of the columnar dendrites. The fact that the transition occurs in a region where both kinds of grains are found, and the estimated size of the new equiaxed grains, suggests that the second situation is more likely to occur. The following arguments reinforce this assumption. During columnar growth, the dynamics of the dendrite are determined by a number of well-known factors such as gradient and growth velocity; however, in the present situation, growth velocity is also a function of temperature

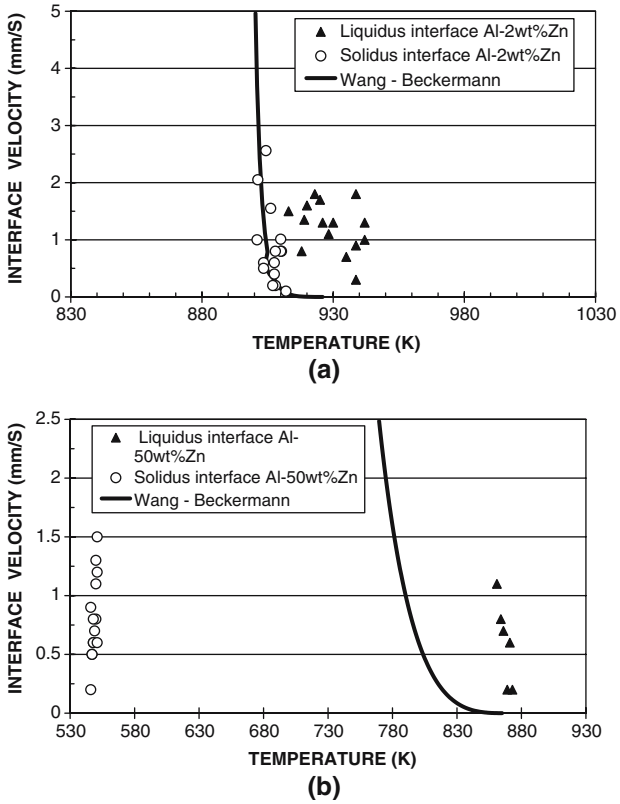

Fig. 17—Interface velocity *vs* temperature for different concentrations of extradendritic liquid. Wang and Beckermann model:[40] (*a*) Al-2 wt pct Zn and (*b*) Al-50 wt pct Zn.

Table III. Thermophysical Properties of Al-Zn and Zn-Al Alloys[39–43,49,50,54,56]

Property Data	Al	Zn	Zn-2 Wt Pct Al*	Zn-4 Wt Pct Al*	Zn-16 Wt Pct Al*	Zn-27 Wt Pct Al*	Al-2 Wt Pct Zn*	Al-4 Wt Pct Zn*	Al-16 Wt Pct Zn*	Al-50 Wt Pct Zn*
Melting temperature, T_M (°C)	660	419.5	—	—	—	—	—	—	—	—
Liquidus temperature, T_L(°C)	—	—	405	390	462	505	657	655	639	572
Solidus temperature, T_S (°C)	—	—	382	382	382	275	650	646	605	275
Partition coefficient, k_0	—	—	0.20	0.20	0.79	0.79	0.43	0.43	0.43	0.43
Liquidus slope, m_L (K wt pct)	—	—	7.52	7.52	−5.90	−5.90	−1.72	−1.72	−1.72	−1.72
Density of the liquid phase, ρ_L(kg/m^3)	2380	6575	6491.1	6407.2	5903.8	5442.3	2463.9	2547.8	3051.2	4477.5
Density of the solid phase, ρ_S(kg/m^3)	2550	6597	6516.1	6435.1	5949.5	5504.3	2630.9	2711.8	3197.5	4573.5
Specific heat of the liquid phase, C_L (J/kgK)	1086	480.0	492.1	504.3	576.9	643.6	1073.9	1061.8	989.1	783.0
Specific heat of the solid phase, C_S (J/kgK)	1123	446	459.6	473.1	554.3	628.8	1109.5	1095.9	1014.7	784.5
Thermal conductivity of the liquid phase, k_L (W/mK)	92	48.5	49.3	50.2	55.4	60.2	91.1	90.3	85.1	70.2
Thermal conductivity of the solid phase, k_S (W/mK)	222	101	104	106	121	134	220	218	203	162
Mass diffusivity of the liquid phase, α_L (m^2/s)	$3.56\cdot10^{-5}$	$1.53\cdot10^{-5}$	$1.57\cdot10^{-5}$	$1.61\cdot10^{-5}$	$1.85\cdot10^{-5}$	$2.08\cdot10^{-5}$	$3.52\cdot10^{-5}$	$3.48\cdot10^{-5}$	$3.24\cdot10^{-5}$	$2.54\cdot10^{-5}$
Mass diffusivity of the solid phase, α_s (m^2/s)	$7.75\cdot10^{-5}$	$3.44\cdot10^{-5}$	$3.52\cdot10^{-5}$	$3.61\cdot10^{-5}$	$4.13\cdot10^{-5}$	$4.60\cdot10^{-5}$	$7.66\cdot10^{-5}$	$7.58\cdot10^{-5}$	$7.06\cdot10^{-5}$	$5.59\cdot10^{-5}$
Latent heat of fusion, λ (kJ/kg)	385	113	118.4	123.9	156.5	186.4	379.6	374.1	341.5	249.0
Liquid/solid surface energy, σ_{SL} (J/m^2)	—	—	$87\cdot10^{-3}$	$87\cdot10^{-3}$	$87\cdot10^{-3}$	$87\cdot10^{-3}$	$169\cdot10^{-3}$	$169\cdot10^{-3}$	$169\cdot10^{-3}$	$169\cdot10^{-3}$
Solute diffusivity, D_L (m^2/s)	—	—	$3.5\cdot10^{-9}$	$3.5\cdot10^{-9}$	$3.5\cdot10^{-9}$	$3.5\cdot10^{-9}$	$3.5\cdot10^{-9}$	$3.5\cdot10^{-9}$	$3.5\cdot10^{-9}$	$3.5\cdot10^{-9}$
Gibbs–Thomson coefficient, Γ (mK)	—	—	$49\cdot10^{-9}$	$49\cdot10^{-9}$	$49\cdot10^{-9}$	$49\cdot10^{-9}$	$49\cdot10^{-9}$	$49\cdot10^{-9}$	$49\cdot10^{-9}$	$49\cdot10^{-9}$

*Calculated

gradient. Near the transition to equiaxed structure, the gradients as well as the velocity are small.

Once the equiaxial grains start to grow after the transition, the velocity of the liquidus front starts to accelerate, and following this, there is nucleation and growth, which is not massive as at the moment of the transition but rather occurs in a continuous or cascade mode. The question at this point is why there is nucleation of new grains rather than growth of these newly formed crystals with fine dendrites. The answer to this relies again in the kinetics of both processes in competition: dendrite growth *vs* nucleation and grain growth. That is, the liquidus front velocity is either the dendrite velocity or the nucleation of new grains, and both must be compatible with the measured velocity.

The velocity for equiaxed dendrites used by Wang and Beckermann[39–43] provides a starting point for the comparison. This velocity is calculated from the following equation:

$$\overline{W}_{me} = \frac{4 \cdot \sigma^* D_l \cdot m \cdot (k-1) \cdot \overline{C}_e}{\Gamma} \cdot \left[a. \left(\frac{\Omega}{1-\Omega} \right) \right] \qquad [1]$$

The velocities given by the preceding equation are represented by the solid line in Figure 17 for two alloy concentrations. The material property values that were used in generating the lines shown in Figure 17 are listed in Table III. In Figure 17, the experimental velocities for the solid and liquid fronts are also represented. It is observed that the prediction from theory is between the experimental velocities for the solid and liquid fronts. According to this, the results are consistent with the view proposed previously in which the liquid front advances faster than the velocity for normal dendritic growth. In such a case, there must always be nucleation of new grains.

Longer columnar length is also more likely to be obtained in cases where the solidification front is formed by fine dendrites such as what is normally expected in higher alloy concentration.

It is interesting to note that this cascade nucleation and growth process applies for the present solidification conditions, which are unidirectional upward and with negligible or no convection. These are not the conditions present during casting where there is substantial convection in the melt and the solidification conditions at the walls differ from those at the bottom.

The more controlled conditions in the present experiment are closer to the conditions present at the bottom of a casting mold. At the initiation of the transition, the mechanism presented here is consistent with the results of Kisakurek[54] and Ares and Schvezov[18,22,45] for lead-tin alloys. However, in a casting, melt flow would not favor a cascade mode for nucleation. Nevertheless, the result obtained here demonstrates that there is no need for nuclei settling at the front coming from broken or dissolved dendrites. Melt flow is expected to produce a washout of nuclei from the front and retardation of the transition and in a sharp plane, until the density and undercooling in the remaining melt are enough to produce the massive nucleation and growth of the equiaxed grains.

V. CONCLUSIONS

From the results and discussion in the previous sections, the main conclusions of this investigation on the CET in aluminum-zinc and zinc-aluminum alloys are as follows.

1. The transition occurs in a zone rather than in a sharp plane, where both columnar and equiaxed grains coexist in the melt.
2. The length of the columnar zone increases with cooling rate and alloy composition, which could be associated with the kinetics of solidification.
3. The temperature gradient, the velocity of the liquidus front, and the heat flux reach low critical values before the transition.
4. In some cases, it is observed recalescence or thermal arrest and negative gradients in the transition zone.
5. After the transition, the speed of the liquidus front accelerates much faster than the speed of the solidus front.
6. The size of the equiaxed crystal is always smaller in the transition zone. The size normally increases afterward. This size distribution also results for other alloys in the literature.
7. It is suggested that the transition is the result of a competition between the growth of the dendrites and the fine equiaxed dendrites in two fields: the thermal and the velocity in which the conditions given at the transition, the equiaxed grains, are more able to grow. The nucleation and solidification of equiaxed grains occur, under the condition present in the experiments, by a cascade mode rather than by massive nucleation and growth in the remaining melt. This is supported by the estimations from theory of velocities for equiaxed dendrites, which are smaller than the measured velocities of the front.
8. The results are consistent with those obtained previously in lead-tin alloys.[18,22,45]

ACKNOWLEDGMENTS

This work was partially supported by CONICET (Consejo Nacional de Investigaciones Científicas y Técnicas, Argentina). The experimental part of this work was developed in the State University of Campinas, Materials Engineering Department, Physic Metallurgy and Solidification Laboratory (Campinas, São Paulo, Brazil). The authors thank Dr. Rubens Caram for the use of his laboratory and equipment and for many helpful suggestions. One of the authors (AEA) is also grateful to C.T. Rios, R.H. Jacon, C. Vieira Leal, S. Gomes da Cruz, F. Gatamorta, J.L. Lisboa, E. Cardoso, F. Pinheiro Martins, and S. Buso Jacon for their technical assistance in the experiments and in the metallographic observations.

LIST OF SYMBOLS

G_L or $G_{(L)}$	temperature gradient in the liquid
G_S or $G_{(S)}$	temperature gradient in the solid
v_L	liquidus velocity
v_S	solidus velocity
T_i	temperature of thermocouple i
$\dot{T}$	cooling rate in °C/min
x_L	liquidus position
C_0	alloy composition
V'	refers to the real interface velocity
m_L	liquidus line slope
k	partition coefficient
Γ	Gibbs–Thomson coefficient
D	liquid diffusion coefficient
$C_p^{(L)}$	specific heat of liquid
α	thermal diffusivity $= k/\rho c_p$
k	thermal conductivity
ρ	alloy density
C_p	specific heat
$\overline{W}_{ne}$	interface velocity of the dendrite envelope in the normal direction to dendritic growth, cm/s
σ^*	stability constant $\approx 1/4\pi^2$ in the limit of pure diffusion
D_l	mass diffusion coefficient in the extradendritic liquid, cm^2/s
$\overline{C}_e$	concentration of chemical species in the dendrite envelope, wt pct $= \frac{T-T_m}{m_L}$
C_L	concentration of chemical species in the extradendritic liquid, wt pct
Ω	solutal undercooling $= \frac{\overline{C}_e - C_l}{\overline{C}_e \cdot (1-k)}$
$a = 0.4567$	
$b = 1.195$	

REFERENCES

1. F.M. Hosking, F. Folgarportillo, R. Wunderlin, and R. Mehrabian: *J. Mater. Sci.*, 1982, vol. 17, pp. 477–98.
2. C.S. Lee, Y.H. Kim, K.S. Han, and T. Lim: *J. Mater. Sci.*, 1992, vol. 27, pp. 793–800.
3. E. Gervais, H. Levert, and M. Bess: *AFS Trans.*, 1980, vol. 88, pp. 183–94.
4. M. Sahoo and L.V. Whiting: *AFS Trans.*, 1984, vol. 92, pp. 861–70.
5. M. Sahoo, L.V. Whiting, and W.G. Whited: *AFS Trans.*, 1985, vol. 93, pp. 475–80.
6. M. Sahoo, L.V. Whiting, and G. Chartrand: *Weatherall. AFS Trans.*, 1986, vol. 94, pp. 225–42.
7. D. Delneuville: *Wear*, 1985, vol. 105, pp. 283–92.
8. R. Auras and C. Schvezov: *Metall. Mater. Trans. A*, 2004, vol. 35A, pp. 1579–90.
9. H. Biloni and B. Chalmers: *Trans. AIME*, 1968, vol. 233, p. 373.
10. S.C. Flood, J.D. Hunt: *ASM Handbook*, ASM, Materials Park, OH, 1998, vol. 15, pp. 130–36.
11. R.B. Mahapatra and F.B. Weinberg: *Metall. Trans.*, 1987, vol. 3 (2), pp. 425–32.
12. S.E. Kisakurek: *J. Mater. Sci.*, 1984, vol. 19, pp. 2289–305.
13. H. Fredriksson and M. Hillert: *Mater. Sci. Technol.*, 1986, vol. 2, pp. 508–14.
14. I. Ziv and F. Weinberg: *Metall. Trans. B*, 1989, vol. 20B, pp. 731–34.
15. S. Kim and R.N. Grugel: *Metall. Trans. A*, 1992, vol. 23A, pp. 1807–15.
16. W.J. Pool and F. Weinberg: *Metall. Mater. Trans. A*, 1998, vol. 29A, pp. 855–61.
17. M.A. Martorano and J.D.T. Capocchi: *Int. J. Cast. Met. Res.*, 2000, vol. 13, pp. 49–57.
18. A.E. Ares and C.E. Schvezov: *Metall. Mater. Trans. A*, 2000, vol. 31A, pp. 1611–25.
19. Ch.A. Gandin: *Acta Mater.*, 2000, vol. 48, pp. 2483–2501.
20. Ch.A. Gandin: *Iron Steel Inst. Jpn.*, 2000, vol. 40, pp. 971–79.
21. C.A. Siqueira, N. Cheung, and A. Garcia: *Metall. Mater. Trans. A*, 2002, vol. 33A, pp. 2107–18.
22. A.E. Ares, S.F. Gueijman, R. Caram, and C.E. Schvezov: *J. Cryst. Growth*, 2005, vol. 275 (1–2), pp. 319–27.
23. V.K. Suri, N. El-Kaddah, and J.T. Berry: *Trans. AFS*, 1991, vol. 99, pp. 187–91.
24. M. Vandyoussefi and A.L. Greer: *Acta Mater.*, 2002, vol. 50, pp. 1693–1705.
25. N. Mangelick-Noel, H. Nguyen-Thi, G. Reinhart, T. Schenk, V. Cristiglio, M.-D. Dupouy, J. Gastaldi, B. Billia, J. Härtwi, and J. Baruchel: *J. Phys. D*, 2005, vol. 38, pp. A28–A32.
26. Ch. Gandin and M. Rappaz: *Acta Metall. Mater.*, 1994, vol. 42, pp. 2233–46.
27. P. Zhu and R. Smith: *Acta Metall. Mater.*, 1992, vol. 40, pp. 683–92.
28. J.A. Spittle and G.R. Brown: *J. Mater. Sci.*, 1989, vol. 23, pp. 1777–81.
29. I. Dustin and W. Kurz: *Z. Metallkd.*, 1986, pp. 265–73.
30. M. Rappaz and Ph. Thevoz: *Acta Metall.*, 1987, vol. 35 (7), pp. 1487–97.
31. M. Rappaz and Ph. Thevoz: *Acta Metall.*, 1987, vol. 35 (7), pp. 1487–97.
32. Ph. Thevoz, J.L. Desbiolles, and M. Rappaz: *Metall. Trans. A*, 1989, vol. 20A, pp. 31–22.
33. P. Zhu and R.W. Smith: *Acta Metall. Mater.*, 1992, vol. 40, pp. 3369–79.
34. J.D. Hunt: *Mater. Sci. Eng.*, 1984, vol. 65, pp. 75–83.
35. J.D. Hunt and S.C. Flood: *Model. Weld. Cast. II*, 1983, pp. 207–13.
36. J.D. Hunt and S.C. Flood: *Model. Weld. Cast. Processes*, 1986, pp. 607–10.
37. M. Gäuman, C. Bezençon, P. Canalis, W. Kurz: *Acta Mater.*, vol. 49, pp. 1501–62.
38. W. Kurz, C. Bezençon, and M. Gäuman: *Sci. Technol. Adv. Mater.*, 2001, vol. 2, pp. 185–91.
39. C.Y. Wang and C. Beckermann: *Metall. Mater. Trans. A*, 1994, vol. 25A, pp. 1081–93.
40. C.Y. Wang and C. Beckermann: *Metall. Mater. Trans. A*, 1996, vol. 27A, pp. 2754–64.
41. C.Y. Wang and C. Beckermann: *Metall. Trans. A*, 1996, vol. 27A, pp. 2765–83.
42. C.Y. Wang and C. Beckermann: *Metall. Trans. A*, 1996, vol. 27A, pp. 2784–95.
43. C.Y. Wang and C. Beckermann: *Miner., Met. Mater. Soc.*, 1997, vol. 49 (3), pp. 13–17.
44. J. Lipton, M.E. Glicksman, and W. Kurz: *Mater. Sci. Eng.*, 1984, vol. 65, pp. 57–63.
45. A.E. Ares, S.F. Gueijman, and C.E. Schvezov: *J. Cryst. Growth*, 2002, vol. 241, pp. 235–40.
46. S. Liu, S. Lu, and A. Hellawell: *J. Cryst. Growth*, 2002, vol. 234, pp. 740–50.
47. M.A. Martorano, C. Beckermann, and C.A. Gandin: *Metall. Mater. Trans. A*, 2003, vol. 34A, pp. 1657–72.
48. G. Kehl: *Fundamentos de la Práctica Metalográfica*, Aguilar, Madrid, 1963, pp. 58–63.
49. *Metals Handbook*, H.E. Boyer and T.L. Gall (eds.), Desk Edition, ASM, Metals Park Ohio, 1985, pp. 1-48, 1-51, 11-1–11-6, 2-19, 2-14, 35-18–35-19.
50. *Metals Handbook*, T. Lyman (ed.), Eight Edition, Vol. 8, ASM, Metals Park Ohio, 1973, pp. 141–42, 264.
51. Ch. A. Gandin and M. Rappaz: *Acta Metall. Mater.*, 1994, vol. 42, pp. 2223–46.
52. G.T. Lowe: Master's Thesis, University of British Columbia, Vancouver, BC, Canada, 1990, pp. 25–62.
53. H. Biloni: *Relación Entre Las Subestructuras de Segregación y Las Estructuras de Fundición*, Departamento de Metalurgia, Comisión Nacional de Energía Atómica, Buenos Aires, Argentina, PMM/R-66, 1971, pp. 36–40.
54. B. Kisakurek: *J. Mater. Sci.*, 1984, vol. 19, pp. 2289–305.
55. B.S. Bokshtein: *Difusión en Metales*, Mir, URSS, 1980, pp. 37–38.
56. W.R. Osório and A. Garcia: *Mater. Sci. Eng. A*, 2002, vol. 325, pp. 103–11.